# A microfluidic device to study cancer metastasis under chronic and intermittent hypoxia

Miguel A. Acosta,[1] Xiao Jiang,[1] Pin-Kang Huang,[2] Kyle B. Cutler,[3] Christine S. Grant,[1] Glenn M. Walker,[1] and Michael P. Gamcsik[2,a)]
[1]*UNC/NCSU Joint Department of Biomedical Engineering, North Carolina State University, 4206D Engineering Building III, 911 Oval Drive, Raleigh, North Carolina 27695-7115, USA*
[2]*Department of Chemical Engineering, National Taiwan University of Science and Technology, No. 43, Sec. 4, Keelung Road, Da'an District, Taipei City 106, Taiwan*
[3]*Department of Biomedical Engineering, Beckman Laser Institute, University of California Irvine, 1002 Health Services Road, Irvine, California 92617, USA*

(Received 2 September 2014; accepted 8 October 2014; published online 17 October 2014)

Metastatic cancer cells must traverse a microenvironment ranging from extremely hypoxic, within the tumor, to highly oxygenated, within the host's vasculature. Tumor hypoxia can be further characterized by regions of both chronic and intermittent hypoxia. We present the design and characterization of a microfluidic device that can simultaneously mimic the oxygenation conditions observed within the tumor and model the cell migration and intravasation processes. This device can generate spatial oxygen gradients of chronic hypoxia and produce dynamically changing hypoxic microenvironments in long-term culture of cancer cells. © *2014 AIP Publishing LLC*. [http://dx.doi.org/10.1063/1.4898788]

## I. INTRODUCTION

The presence of large regions of hypoxic tissue within tumors is a demonstrated indicator of poor patient outcomes.[1] Hypoxic tissue within tumors, however, can be static (chronic) or dynamic, with constantly changing oxygen partial pressures.[2] These dynamic changes are referred to as cycling or intermittent hypoxia. Chronic hypoxia is caused by poor oxygen diffusion from tumor vasculature and surrounding tissues, whereas intermittent hypoxia is caused by cyclical fluctuations of blood flow to the tumors.[3] Both chronic and intermittent hypoxia can have very different effects on the aggressiveness and survival of migrating cells. For example, Pires *et al.*,[4] showed that re-oxygenation after chronic hypoxia can cause DNA damage and inhibit replication and tumor progression, whereas intermittent hypoxia can increase genomic instability. In addition, Jessup *et al.*[5] reported that re-oxygenation can kill weakly metastatic cells. *In vivo*, metastatic cells must migrate from the hypoxic tumor and enter the normoxic vasculature while being exposed to significant gradients in oxygen concentration that may affect their survival.

Studies of intermittent hypoxia *in vivo* rely upon placing entire animals within environmental chambers with altered oxygenation levels that enhance metastasis and leads to poor outcomes.[6] However, tumor oxygen content is difficult to assess and to control in these models. There is a need, therefore, for an *in vitro* platform that can provide dynamic oxygenation control, recreating either chronic and/or intermittent hypoxia, while simultaneously assessing the invasive capability of cells. The chemo-invasion assay is an established method for studying the invasive capabilities of tumor cells.[7] It simulates tumor cell invasion through the extra cellular matrix (ECM) tissue barriers using a Boyden chamber. Although Boyden chambers with inserts to create hypoxia have been developed,[8] migrating cells in these designs do not experience oxygen gradients similar to what occurs during the intravasation process *in vivo*.

a)Author to whom correspondence should be addressed. Email: mgamcsi@ncsu.edu.

 

Furthermore, no *in vitro* models have been developed that can mimic clinically observed cycles of intermittent hypoxia.

Microfluidic technologies have been successfully employed as tools for studying cell migration and tumor cell metastasis.[9–19] This includes devices to study chemotaxis,[13,19] drug responses,[12] and drug resistance.[16] In addition, microfluidic technologies can easily be adapted to measure the influence of other cells[11,15,17,18] or varying electric fields[14] on cell migration. Of particular interest is the work of Chaw *et al.*,[9,10] who developed a microfluidic device that comprised two channels connected by narrow migration portals plugged with an ECM membrane. Cell migration in response to the presence of a chemo-attractant could be easily monitored with microscopy, creating a micro-scale system very similar to a conventional Boyden chamber.

Microfluidic technologies can also elegantly integrate both temporal and spatial control of oxygen concentrations with a variety of methods. Placing microdevices inside environment chambers with controlled gas flow can achieve chronic hypoxia[20,21] or cycles to model ischemia/reperfusion injury.[22] Temporal control of oxygen concentration also has been achieved with the inclusion of gas channels either overlying,[23,24] or underneath[25,26] the cell culture channels. Similarly, spatial control of oxygen concentration has been achieved with the inclusion of gas channels adjacent to[27–29] and overlying[30] the cell culture channels. Cellular oxygen consumption has also been used to generate oxygen gradients in single-[31] and multi-layer[32] devices and in multicellular aggregates.[33] Furthermore, spatial gradients have been achieved by chemical control[34] and electrolytic control of oxygen concentration.[35] Lo *et al.*,[26] demonstrated oxygen control to study calcium signaling and insulin kinetics of islet cells with intermittent hypoxia cycles of 1 min.

We sought to adapt the aforementioned technologies to create a tumor-on-a-chip microfluidic device that combines temporal and spatial oxygen control with an invasion assay with the goal of assessing the effect of chronic and intermittent hypoxia on metastatic cancer cell lines. Herein, we present the device's design, demonstrate that it can generate the desired oxygen temporal patterns and spatial gradients, and maintain cells in long-term culture. These devices allow for future comparative studies of the effects of chronic and intermittent hypoxia in tumor cell models.

## II. MATERIALS AND METHODS

All reagents were purchased from either Fisher Scientific (Pittsburgh, PA), or Sigma-Aldrich (St. Louis, MO), unless otherwise stated.

### A. Preparation of oxygen-sensing microparticles

The oxygen-sensing microparticles were prepared as described by Acosta *et al.*[36] However, for the particles presented here, no reference luminophore was employed. Briefly, 2 g of silica gel (Davisil, grade 710) was stirred in 40 ml of 0.01 N NaOH for 30 min. Then, 10 ml of a 0.05 mM solution of the oxygen-sensitive luminophore tris-(4,7-diphenyl-1,10-phenanthroline) ruthenium (II) dichloride, or $Ru(Ph_2phen_3)Cl_2$ (GFS Chemicals, Powell, OH), in pure ethanol was added to the suspension and stirred for an additional 30 min. Next, the suspension was centrifuged for 5 min at 500 g, and the supernatant was removed. The particles were washed and centrifuged three times with 30 ml of deionized water and once with 30 ml of pure ethanol. After the ethanol wash, the particles were oven dried at 70 °C overnight and later stored in the dark.

### B. Microfluidic device design and fabrication

Fabrication of the microfluidic device was performed by replica-molding poly(dimethylsiloxane) (PDMS, Sylgard 184) from SU-8 photoresist (MicroChem Corp., Newton, MA) patterned on a silicon wafer. The device comprised two layers of replica-molded PDMS, as shown on Fig. 1. The first layer, the cell-channel layer, consisted of three channels with dimensions of 3 cm × 400 $\mu$m × 50 $\mu$m (L × W × H, respectively), separated by a series of 50 $\mu$m × 50 $\mu$m posts

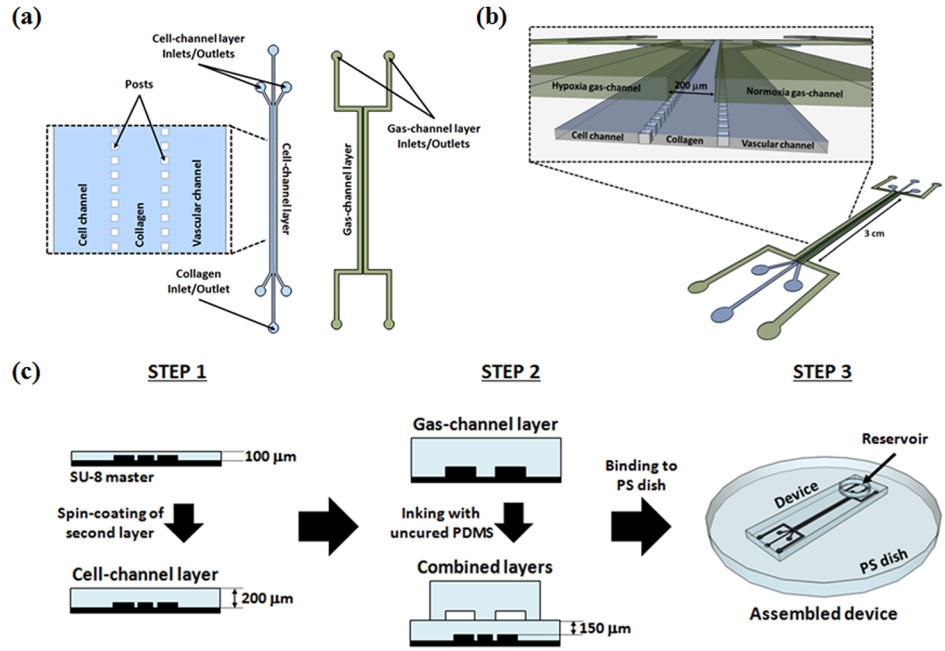


FIG. 1. (a) Schematic of photoresist master patterns. The enlarged diagram shows the $50 \times 50\,\mu$m posts along cell-channel layer length. (b) Isometric view of combined cell- and gas-channel layers. The enlarged diagram shows a cross-section indicating the cell and vascular channels and the gas channels used for delivery of the hypoxia and normoxia gas mixtures. (c) Schematic of the device fabrication process. Step 3 displays the microfluidic device bound to PS dish and the circular reservoir bound atop of the device to hold cell medium for withdrawal and maintenance of the cells during culture.

with a pitch of $50\,\mu$m. The posts helped hold the basement membrane gel in the middle channel. The second layer, the gas-channel layer, consisted of two channels with dimensions of $3\,\text{cm} \times 800\,\mu\text{m} \times 100\,\mu\text{m}$ ($\text{L} \times \text{W} \times \text{H}$, respectively), separated by $200\,\mu$m. SU-8 masters for both cell- and gas-channel layers were treated with trichloro(octyl)silane, by vapor deposition, to facilitate removal of PDMS replicas and extend master lifetime.

The cell-channel layer was fabricated by spin-coating PDMS at 890 rpm for 1 min on the cell-channel master and then curing it for 1 h at 90 °C. A second layer of PDMS was then spun on top of the first at the same rate and cured at the same conditions, resulting in a layer with a total thickness of $200\,\mu$m. The gas-channel layer was an arbitrary thickness and was prepared also by curing PDMS on the gas-channel master for 1 h at 90 °C. A third, blank, wafer was spin-coated with uncured PDMS at 5000 rpm for 1 min. The gas-channel layer was removed from its master, cut to size, punctured for tubing connections, and then gently pressed on the third wafer to ink it with the uncured PDMS. Then, it was aligned on top of the cell-channel layer by stereoscope. After alignment, the construct was cured at room temperature for 1 h, prior to baking for another hour at 90 °C, to prevent drifting and misalignment. Finally, a circular PDMS reservoir with dimensions of $1\,\text{cm} \times 1.5\,\text{cm}$ ($\text{H} \times \text{D}$, respectively) was bound to the top of the completed device using the PDMS stamping procedure above.

For empirical characterization of oxygen transport, the completed devices were plasma bonded to a $200\,\mu$m thick PDMS film, containing the oxygen-sensing microparticles. This oxygen-sensing layer was fabricated by first spin-coating PDMS at 890 rpm for 1 min on the surface of a blank wafer, and curing at 90 °C for 1 h to yield a $100\,\mu$m layer. Next, a 2:1 solution of PDMS diluted in hexane, containing 0.2 g/ml of the oxygen-sensing microparticles, was spin-coated at 890 rpm for 1 min and cured at 90 °C for 1 h on top of the first layer. The final device, containing the particle layer, was subsequently bound to a polystyrene (PS) cell culture dish using a modified protocol based on Sunkara *et al.*,[37] and Hwang *et al.*[38] Briefly, a PS cell culture dish was plasma treated and immediately coated with a 1% (v/v) solution of (3-aminopropyl)triethoxysilane (APTES). After 20 min, the dish was rinsed thoroughly with pure ethanol and dried with compressed air. Next, the PDMS microfluidic device was plasma treated and

immediately bound to the APTES-treated dish. The construct was then baked at 70 °C for 2 h. Devices fabricated for cell culture experiments did not contain the 200 $\mu$m microparticle film and were bound directly to the PS dish.

### C. Finite element analysis of oxygen mass transfer

COMSOL Multiphysics software was used to create 2D models of oxygen transport within the tumor-on-a-chip device. Specifically, the models were for transport across the cross-section of the device. The "Transport of Diluted Species" toolbox was used for the model. Furthermore, the model was constructed with the assumption that the device was under steady-state, i.e., the oxygen concentrations within the device did not change with time. Boundary conditions for the model were: (1) there is oxygen flux through the outside walls of the PDMS out to the atmosphere, and (2) there is oxygen flux through the interface between the PDMS and the PS dish. Values for oxygen diffusivity in water, PDMS, air, and PS and initial concentrations of oxygen in the gas mixtures are presented in Table I. The collagen gel was assumed to have the same oxygen diffusivity as water. Additionally, the initial concentration of oxygen within the collagen gel was assumed to be equivalent to the saturation value for oxygen in water at room temperature. Two models were constructed: one for a device bound directly to the PS dish, to simulate conditions during cells culture; and a second for a device with the 200 $\mu$m thick film of PDMS containing oxygen-sensing microparticles.

### D. Collagen gel loading

The middle channel of the cell-channel layer was filled with a collagen gel to mimic an *in vivo* ECM. Rat tail type I collagen was diluted to a concentration of 2 mg/ml in a solution composed of water and 10% (v/v) 10× Hank's balanced salt solution. The solution was kept on ice and titrated to a basic pH with 0.1M NaOH. Immediately after titration, the collagen solution was loaded into a 1 ml syringe, without a plunger, and connected to the device via Tygon tubing (Cole Parmer, Vernon Hills, IL). The collagen was infused into the middle channel by slightly elevating the syringe above the level of the device to increase hydraulic pressure. After filling, the device was incubated for 30 min at room temperature, and then placed in the cell culture incubator for an additional 90 min to complete gel formation.

### E. Empirical characterization of oxygen mass transfer

Once the middle channel was filled with collagen, the cell and vascular channels were filled with phosphate buffered saline (PBS) by gravity feed. Gas was delivered to the upper gas channels at a rate of 5 ml/min and a syringe pump was used to infuse PBS through the lower channels at a rate of 2 $\mu$l/min for 30 min. Gas and PBS flow was concurrent. This initial priming step served to remove any bubbles that remained within the device after filling. Once bubbles were removed from the device, it was transferred to the stage of a fluorescence microscope

TABLE I. Constants used for the COMSOL model of oxygen transport within the tumor-on-a-chip device.

| Parameter | Value | Description |
|---|---|---|
| $D_{O2,\ W}$ | $2.1 \times 10^{-5}$ cm$^2$/s | $O_2$ diffusivity through water |
| $D_{O2,\ PDMS}$ | $4.1 \times 10^{-5}$ cm$^2$/s | $O_2$ diffusivity through PDMS[39] |
| $D_{O2,\ A}$ | 0.175 cm$^2$/s | $O_2$ diffusivity through air |
| $D_{O2,\ PS}$ | $2.3 \times 10^{-7}$ cm$^2$/s | $O_2$ diffusivity through PS[40] |
| $C_{O2,\ W}$ | 8.32 mg/l | Saturation concentration of $O_2$ in water |
| $C_{HYP}$ | 7.6 mm Hg, 16 mm Hg, 38 mm Hg | $O_2$ partial pressures used in hypoxia channel. 1%, 2%, and 5% $O_2$, respectively |
| $C_{O2,\ A}$ | 160 mm Hg | $O_2$ partial pressure used in normoxia channel, 21% $O_2$ |

(Olympus IX-71; Olympus, Center Valley, PA). During characterization experiments, PBS flow rate was reduced to 0.1 $\mu$l/min.

Mass flow controllers (Aalborg, Orangeburg, NY), under LabView direction, were used to deliver gas flow in the normoxia and hypoxia gas channels. Two controllers were used to mix two gases off-chip, a gas containing 95%-$N_2$/5%-$CO_2$ and another containing 21%-$O_2$/74%-$N_2$/5%-$CO_2$, in appropriate proportions. A third controller was used to flow 21%-$O_2$/74%-$N_2$/5%-$CO_2$ through the normoxia channel during experiments where gradients within the device were generated. Gas flow rates in both gas channels on-chip were maintained at 5 ml/min.

The oxygen-sensing microparticles were calibrated by generating step increases in oxygen concentration and measuring their changing fluorescence intensities. After each step-change, a 5 min interval was allowed to enable the system to equilibrate. Five fluorescence images of the microparticles were captured using a 1100 v3 UV filter set (Chroma Technology Co., Bellows Falls, VT), at 6.4× magnification, 20 s apart. Excitation and emission wavelengths for $Ru(Ph_2phen_3)Cl_2$ are 470 and 610 nm, respectively. This time-lapse imaging was repeated after each step-change in oxygen concentration. Images captured the entire width of the cell-channel layer and the underlying microparticles. Three replicate calibrations were performed, each in a randomly chosen location of the device. Image analysis was conducted using NIH-ImageJ. Line scans across the length of all images were used to calculate the average values of microparticle fluorescence intensity. The average values of intensity represented a global measurement of intensity across the area of the image.

Oxygen diffusion from the gas channels will cause changes in the fluorescence intensity of the $Ru(Ph_2phen_3)Cl_2$ containing particles in accordance with the Stern-Volmer model. In this study, the two-site Stern-Volmer model was used,

$$\frac{I_0}{I} = \left(\frac{f_1}{1 + K_{SV1}[O_2]} + \frac{f_2}{1 + K_{SV2}[O_2]}\right)^{-1}, \tag{1}$$

where $I_0$ and I are the fluorescence intensities of $Ru(Ph_2phen_3)Cl_2$ in the absence and presence of oxygen, respectively. This model, proposed by Carraway *et al.*,[41] is required when an oxygen-sensitive luminophore, such as $Ru(Ph_2phen_3)Cl_2$, is immobilized within a polar carrier that is distributed through a non-polar polymer matrix. The luminophore is divided into two populations, a quenchable and an unquenchable population, with molar fractions ($f_1$ and $f_2$, respectively) and associated quenching constants ($K_{SV1}$ and $K_{SV2}$, respectively). Generally, the quenching constant for the unquenchable population ($K_{SV2}$) is assumed to be very small, and the two molar fractions are additive ($f_1 + f_2 = 1$). This simplifies Eq. (1) to

$$\frac{I_0 - I}{I_0(f_1 - 1) + I} = K_{SV}[O_2]. \tag{2}$$

Equation (2) is a simpler two-parameter fit and results in a direct relationship between the known oxygen concentrations and the fluorescence response from the microparticles. Microparticles were calibrated prior to each experiment. After the calibration measurements, gas flow was changed to generate an oxygen gradient within the device. The gas mixture containing only 21% $O_2$ was delivered to the normoxia channel, and gas mixtures containing 1%, 2%, or 5% $O_2$ (hypoxia) were delivered to the hypoxia channel. Five fluorescence images were captured 20 s apart. Image analysis was performed in the same manner as described above. The two-site Stern-Volmer calibration was used to convert fluorescence intensity to oxygen partial pressure and to compare the measured oxygen gradients in the device to the COMSOL model.

### F. Cell culture experiments

PANC-1 (pancreatic adenocarcinoma) cells were maintained with Dulbecco's modified Eagle's medium (DMEM), supplemented with 10% (v/v) fetal bovine serum (FBS) and 1% (v/v) penicillin/streptomycin. Cell growth was compared in the microfluidic device and in

conventional cell culture flasks. For the latter, PANC-1 cells were seeded to an initial density of approximately 2000/flask within T-25 flasks and incubated in an atmosphere of air/5% $CO_2$ at 37 °C. Cells were harvested with trypsin and counted each day for 8 days using a Trypan blue exclusion assay. Three replicates were performed.

All tumor-on-a-chip devices used for cell culture experiments were bound directly to PS dishes, sterilized with 70% ethanol, and baked for 2 h at 70 °C, prior to collagen gel loading and cell seeding. Once the collagen gelled, both the cell channel and the vascular channel were filled with medium by gravity feed from Tygon tubing connected to their respective inlets. To seed the cells, a suspension of $1 \times 10^6$ cells/ml was added to the reservoir. Gravity driven flow, in the opposite direction to how the medium was loaded, was continued for 2 min, after which the tubing was clamped and the reservoir was washed free of the cell suspension and reloaded with fresh medium. The devices were transferred to the $CO_2$ incubator, and the cells were allowed to settle and adhere for 4 h. After attachment, medium was withdrawn from the circular reservoir at a rate of 0.1 $\mu$l/min by syringe pump to maintain the cells. Initial cell number was obtained by microscopic examination. For normoxia experiments, no gas flow was used, as the device equilibrated with the atmosphere within the air/5%$CO_2$ incubator. For the hypoxia experiment, a gas mixture of 1% $O_2$ was delivered to the gas channel above the PANC-1 cells. Air was delivered to the gas channel over the vascular side containing only growth medium. Cell counts were obtained from microscopic examination of the entire length of the cell-channel for 8 days. Three replicates of each condition of oxygenation were performed. The specific growth rate ($\mu_{\text{net}}$) of the cells was compared in the device, both for normoxic culture and while in the presence of an oxygen gradient, and in conventional cell culture flasks. The specific growth rate of a culture is defined as

$$\ln\left(\frac{\mathrm{N}}{\mathrm{N}_0}\right) = \mu_{net} t, \tag{3}$$

where $N_0$ and N are the cell numbers at $t_0$ and $t_n$, respectively, and $t$ is the time measured in hours. A logarithmic plot of each culture's growth curve was used to identify its exponential growth phase, which is later subject to linear regression. The specific growth rate is the slope of this regression. Subsequently, the doubling times ($\tau_d$) for the cultures were determined from

$$\tau_d = \frac{\ln(2)}{\mu_{net}}. \tag{4}$$

The percentage of cells present in the collagen and vascular channel was calculated from the number of cells within these channels divided by total number of cells within the device, multiplied by 100.

### G. Statistics

The two-site Stern-Volmer calibration of the oxygen-sensing microparticles is presented as mean ± standard error of the mean (SEM). All remaining data are presented as mean ± standard deviation (STDEV). Specific growth rates for cell experiments were compared with an analysis of variance (ANOVA) and a Student's $t$-test, for pair-wise comparisons, both at $p < 0.05$. Migration and intravasation percentages were also compared with a Student's $t$-test, $p < 0.05$.

## III. RESULTS AND DISCUSSION

The current design of the tumor-on-a-chip device is an adaptation of previously reported microfluidic technologies for invasion/migration assays.[9,10,15] Initially, the cell layer was designed by adapting the invasion device of Chaw *et al.*,[10] with narrow migration channels directing cell movement, but this required multi-layered microfabrication protocols. Additionally, since another goal of our studies is to determine the effect of the oxygen gradients on directed migration of cells,[29] the design of Huang *et al.*[15] became a subsequent starting

point. In his design, two parallel channels are separated by an ECM-filled channel defined by a series of hexagonal posts that will allow directional mobility for migrating cells. Adapting this design proved to be advantageous as it simplified the fabrication of the cell-channel layer master.

None of the previously reported devices for invasion/migration assays, however, were designed to incorporate the capability for oxygen spatial or temporal control. An important initial design criterion was that the cells be exposed to a uniform oxygen partial pressure across the width of the channel. Here we define uniformity as all oxygen partial pressures within the channel are within 10% of the mean. Although there are many options for controlling oxygen levels in microdevices, the design using gas channels positioned above the cell channel[23,24] was adapted to offer the most uniform oxygen content. With these initial designs for the device, computational modeling of oxygen mass transport was used to determine the optimal dimensions and orientations of cell, migration, vascular, and gas channels.

### A. Finite element analysis of oxygen mass transfer

The goal was to create two cell culture channels; one that could experience chronic or intermittent hypoxia over its entire width, and another that could be maintained at normoxia. The middle channel would then contain an oxygen gradient. Initial models tested the mass transfer characteristics of a device in which the gas channel width was equal to the cell channel width.

The oxygen concentration profile across the cell channel width in this device shows little uniformity (see supplementary material, Fig. S1[42]). Widening the gas channel but maintaining a 400 $\mu$m gap between the channels improved the uniformity of the oxygen profile (see supplementary material, Fig. S2[42]). However, in this design, the profile of the right half of the cell channel between the 400 and 600 $\mu$m positions varied too widely. Through interactive refinement of the models, the optimum width for the gas channels was found to be 800 $\mu$m, with a separation of 200 $\mu$m between the two. This width provided a good balance between uniform oxygen concentrations within the cell and vascular channels and a near linear gradient through the collagen gel. A separation of less than 200 $\mu$m made the oxygen gradients very steep, while even wider gas channels, $>$800 $\mu$m, would necessitate widening of the collagen channels to distances that would impede diffusion of molecules (e.g., cytokines) from the vascular to cell channel.

We modeled the distribution of oxygen within the device when gas containing 1%, 2%, and 5% $O_2$ was delivered through the hypoxia channel and the normoxia channel was maintained at 21% $O_2$. Fig. 2(a) shows a map of the oxygen partial pressure throughout the device when 1% $O_2$ is delivered through the hypoxia channel. The models were evaluated by plotting partial pressures along the bottom surface of the cell-channel layer, where cells would be seeded. The gas mixtures within the hypoxia channel, 1%, 2%, and 5% $O_2$, correspond to partial pressures of 7.6, 15.2, and 38 mm Hg, respectively, and the gas delivered to the normoxia channel, 21% $O_2$, corresponds to 160 mm Hg. The surrounding atmosphere was set to 21% $O_2$. The predicted oxygen gradients at the cell-channel layer surface for all three levels of hypoxia are shown in Fig. 2(b). For all three oxygen concentrations, 75% of the cell channel width experiences a standard deviation in oxygen partial pressure of less that 10% ($9.1 \pm 0.6$, $17.4 \pm 0.6$, and $39.2 \pm 0.5$ mm Hg for 1%, 2%, and 5% $O_2$, respectively), demonstrating that the device can generate a uniform hypoxic microenvironment for cells. The model shows that the region of the cell channel between the positions of 500 and 600 $\mu$m (Fig. 2), adjacent to the collagen, would show the largest variation in oxygen partial pressure levels due to its proximity to the normoxic atmosphere over the vascular channel. An approximately linear increase in oxygen partial pressure from hypoxia to normoxia over the width of the migration channel is evident from the models, demonstrating that the device creates the desired spatial oxygen gradients.

Despite the diffusivity of oxygen through PS being two orders of magnitude lower than that for PDMS, the models predict that there is some loss of oxygen through the PS dish.

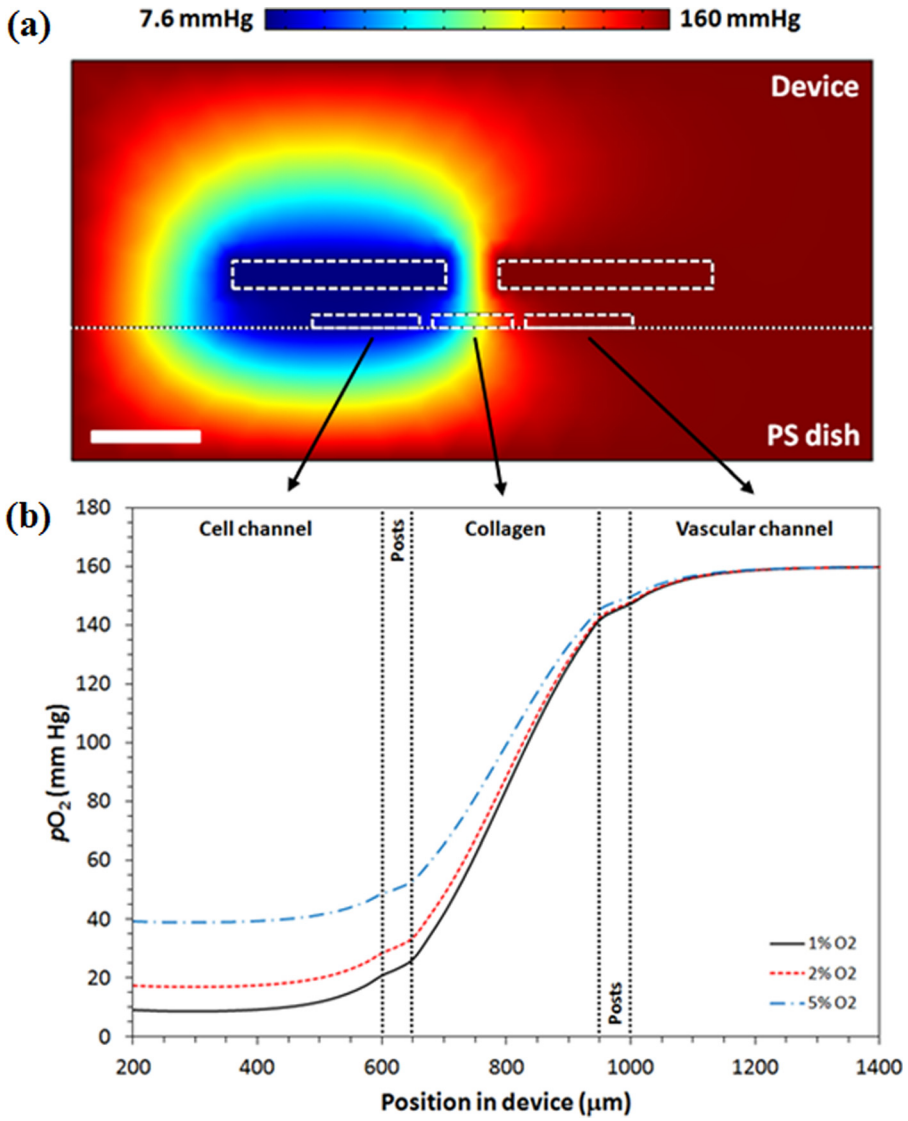


FIG. 2. (a) Oxygen concentrations at steady-state within cross-section of the microfluidic device bound to PS dish. The oxygen content in the hypoxia and normoxia channels is 1% and 21% respectively. Scale bar marks 400 $\mu$m. (b) Predicted oxygen partial pressure gradient across the width of cell-channel layer of device bound directly to a PS dish. The theoretical oxygen gradient was obtained with a line profile at the interface between the device and the PS (represented by the dotted white line).

Randers-Eichhorn *et al.*,[43] found that oxygen penetrating through the walls of a standard PS flask supplies 30% of the oxygen to cells. Therefore, the permeability of PS cannot be ignored in the model, even with its low diffusivity. Additionally, for the constructed models, the collagen gel was assumed to have the same oxygen diffusivity as water. Data are scarce for diffusivity of oxygen through any type of collagen gel; particularly for a 2 mg/ml gel. For a 3 mg/ml solution, previous researchers have used values in the range of $0.6–2.5 \times 10^{-5}$ $cm^2/s$.[44] There is no evidence of oxygen molecules interacting chemically with collagen fibers in its hydrogel form. Hence, the only likely interaction that oxygen could have with the collagen is through physical collisions with fibers, which is influenced by protein concentration. Therefore, the higher end of this diffusivity is a good estimate for a 2 mg/ml gel, which is the value we used for both water and collagen ($2.1 \times 10^{-5}$ $cm^2/s$, as reported in Table I).

### B. Device fabrication and collagen filling

Fig. 1 shows detailed schematics of our device design, including post location and spacing. The middle channel of our device is defined by 50 $\mu$m posts, separated by 50 $\mu$m gaps, in order to leave sufficient room for cell migration and still create enough surface tension to allow for gravity-induced loading of the collagen solution. In our trials, we found gravity loading of the gel solution to be considerably more reliable than injection loading.

Unlike previous on-chip invasion devices, the application of flowing gas created unique problems with medium perfusion. During assembly, the devices were primed by infusing buffer or medium through the cell channel while gas was flowing through the overlying gas channels. After the lower channels were filled with liquid, small air pockets remained trapped in between the posts. During early experiments, we observed that gas flow through the top gas channels would generate bubbles within the cell channels as a result of the presence of these air pockets. Therefore, priming the device by infusing medium/buffer at a rate of 2 $\mu$l/min for 30 min under the presence of flow through the gas channel eliminated the air pockets, and any bubbles formed from them, post-gel loading.

### C. Oxygen sensing across the cell, collagen, and vasculature channels

Once fabricated, several approaches were explored to measure the oxygen concentration within the cell-channel layer. Initially, the cell-channel layer was filled with water containing the soluble oxygen-sensing luminophore tris-(2,2″ bipyridine) ruthenium (II) chloride hydrate, but the quantum yield was too low (data not shown), precluding accurate assessment of oxygen variability across the device. Alternatively, oxygen sensor coated glass slides (e.g. FOXY slides; Ocean Optics, FL) were evaluated, but the non-uniform coating of these slides did not have the spatial resolution necessary to chart the oxygen homogeneity across the device. Finally, oxygen-sensing microparticles were used. These needed to be immobilized in the vicinity of the channels and uniformly distributed across the device. To meet these requirements, the microparticles were embedded within a 200 $\mu$m thick PDMS film below the cell-channel layer. The $Ru(Ph_2phen_3)Cl_2$ luminophore used in this study is a polar molecule and does not dissolve and distribute evenly in the PDMS film. Therefore, it was immobilized on a silica carrier that acts to maintain its charged, oxygen-sensing state,[36] and allows uniform distribution of the suspended particles within the 200 $\mu$m thick PDMS film below the cell-channel layer. Although this significantly modified the initial design, the high quantum yield and uniform distribution of these particles proved appropriate for accurate oxygen measurements and outweighed the disadvantage of including a 200 $\mu$m thick layer.

To determine the effect of adding a 200 $\mu$m thick PDMS layer on oxygen transport properties, a separate COMSOL model was created. Fig. 3(a) shows a heat map for a device bound to the microparticle containing PDMS film. Both heat maps shown in Figs. 2(a) and 3(a) are for 1% $O_2$ in air. The heat maps from models corresponding to 2% and 5% $O_2$ are similar, and therefore not shown. Fig. 3(a) shows a larger hypoxic region below the gas channel compared to that in Fig. 2(a). Similarly, Fig. 3(b) demonstrates that the addition of the microparticle film changes the oxygen transport properties of the device, reducing the uniformity across the channels, and exhibiting a broader gradient between the cell and vasculature channels. The change in the predicted gradient is expected, as the PDMS film below the cell-channel layer allows for increased oxygen penetration from the surrounding atmosphere. Although inclusion of this thick PDMS film containing the microparticles is not ideal, the sensing capabilities allowed for good sensitivity and resolution of the oxygen gradients across the device.

### D. Stern–Volmer calibration of oxygen-sensing microparticles

Oxygen sensors based off of fluorescence collisional quenching by oxygen of ruthenium analogs and porphyrins have been employed in a host of applications, ranging from microfluidic devices, fermentation, and for measurements of oxygen gradients in engineered tissues.[45–48] These sensors are used in place of conventional Clark-type electrodes due to their adaptability,

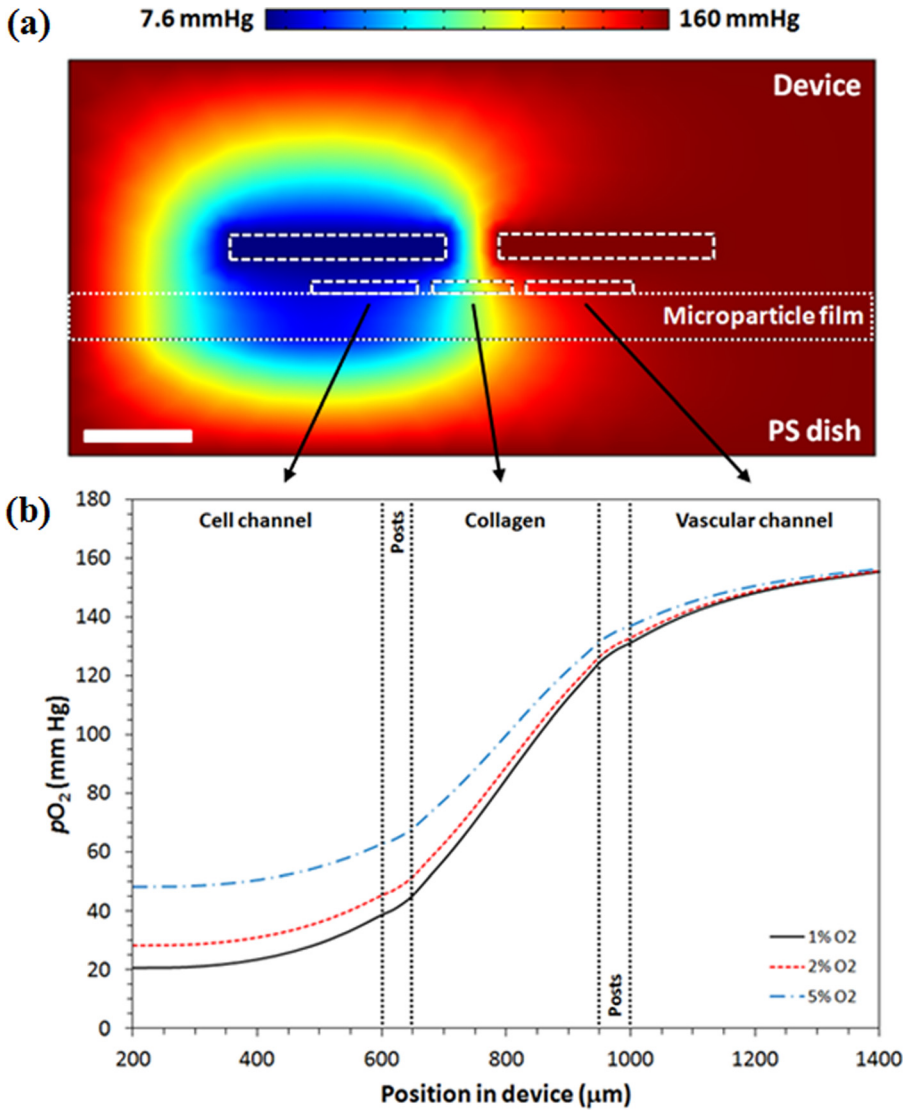


FIG. 3. (a) Map of oxygen concentrations at steady-state within cross-section of microfluidic device bound to 200 $\mu$m PDMS film containing the oxygen-sensing microparticles. The oxygen content in the hypoxia and normoxia channels is 1% and 21%, respectively. Scale bar marks 400 $\mu$m. (b) Predicted oxygen partial pressure gradient across the width of cell-channel layer of device bound microparticle containing PDMS film. As with the PS model, a line profile was used at the interface between the device and the film (represented by top line of the dotted rectangle marking the microparticle film) to create this figure.

rapid response to changing oxygen and their non-invasiveness; i.e., they do not consume oxygen during operation. We chose $Ru(Ph_2phen_3)Cl_2$ due to its high quantum yield and stability at low oxygen concentrations. The calibration of the oxygen-sensing microparticles was performed by combining oxygen and nitrogen, both containing 5% $CO_2$, in step-wise increments and delivered through the gas channels. Oxygen concentrations within the cell-channel layer were monitored by capturing fluorescence images of the sensing microparticles housed within a 200 $\mu$m thick film of PDMS. The microscope was focused on the layer of microparticles immediately below the cell channel. The focal plane and location were not changed between the calibration and characterization data collection. The correlation of oxygen content and fluorescence intensity from the captured images was obtained by using the two-site Stern-Volmer model. Fig. 4(c) shows the calibration. Regression results were $0.0087 \pm 0.0008$ (mm Hg)$^{-1}$ for the Stern-Volmer quenching constant ($K_{SV}$) and 0.9979 for the coefficient of determination ($R^2$), which

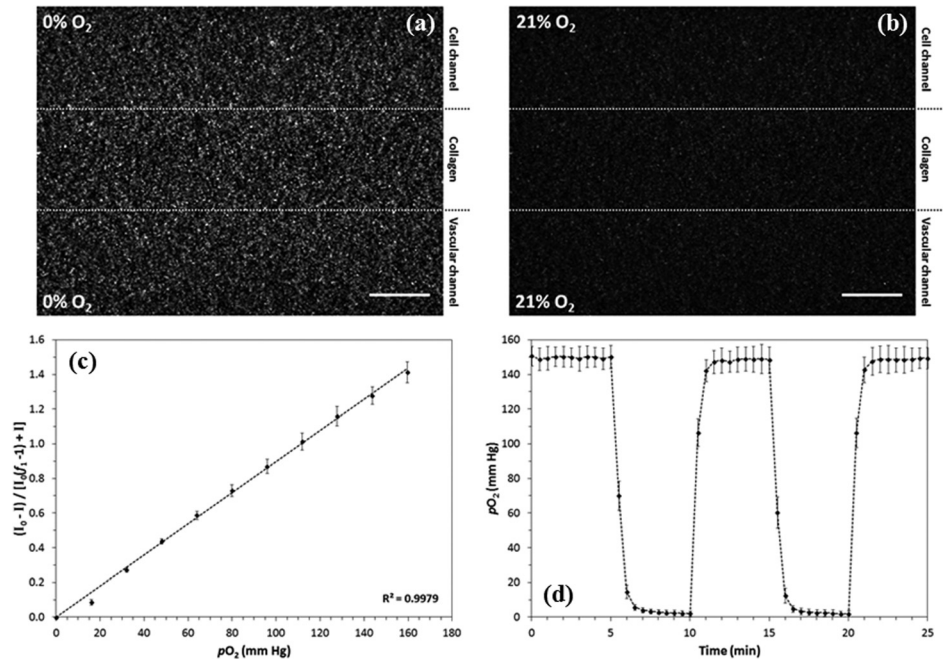


FIG. 4. Fluorescence images of oxygen-sensing microparticles embedded within 200 $\mu$m PDMS film for (a) 0% $O_2$ and (b) at 21% $O_2$ at 6.4× magnification. Scale bar marks 200 $\mu$m. (c) Calibration of microparticle film using two-site Stern–Volmer model ($R^2 = 0.9979$). Calibration data shown as mean ± standard error of the mean for the three replicates (n = 3). (d) Reversibility response of oxygen-sensing microparticles within the PDMS film. Reversibility data shown as mean ± standard deviation for the three replicates (n = 3).

demonstrates a linear model. The value obtained for the quenchable luminophore fraction ($f_1$) was 0.92 ± 0.02, stating that approximately 92% of the $Ru(Ph_2phen_3)Cl_2$ luminophore is available for quenching during our experiments. This value is very close to that previously reported for $Ru(Ph_2phen_3)Cl_2$ immobilized within silica gel and later dispersed within PDMS films.[41] Most importantly however, Fig. 4(c) shows that the particles within the PDMS film are capable of measuring oxygen partial pressures relevant to those to be employed for the characterization of the microfluidic device.

### E. Empirical characterization of oxygen mass transfer

Characterization of the microfluidic device was performed by delivering a gas mixture containing low oxygen (1%, 2%, and 5% $O_2$) into the hypoxia gas channel and 21% $O_2$ into the normoxia gas channel. Oxygen concentration was monitored by capturing fluorescence images from the underlying microparticle film. Fig. 4(a) shows fluorescence from the particles at 0% $O_2$ infused through both gas channels, and Fig. 4(b) shows fluorescence from the particles at 21% $O_2$ infused through both gas channels.

As expected, oxygen quenches fluorescence from the microparticles, leading to diminished intensity, which is evident in Fig. 4(b). Fluorescence intensity was converted to oxygen partial pressure by using the two-site Stern–Volmer calibration shown in Fig. 4(c). The temporal response of the device is important for recreating intermittent hypoxia patterns analogous to those observed in clinical tumors. Intermittent hypoxia within murine and human tumors has been shown to occur for periods ranging between 20 min to 2 h.[49–51] Reversibility experiments performed with the microparticle film (Fig. 4(d)) demonstrate the fast diffusion times within the device and the stability of the microparticles within environments with varying oxygen concentrations. In addition, Fig. 4(d) demonstrates that the steady-state assumption we chose for the computational models is valid, as the oxygen content sensed by the microparticles equilibrates within 2 to 3 min after a change in concentration. The data in Fig. 4(d) also demonstrates that

the fluorescence intensity of particles at a given oxygen concentration was stable during the course of the experiments and, therefore, did not photobleach. Fig. 5(a) shows the fluorescence from the particles in response to a gradient generated by infusing 1% $O_2$ through the hypoxia gas channel parallel to 21% $O_2$ within the normoxia gas channel. Figs. 5(b)–5(d) show the results of the measured spatial gradients in oxygen concentration, compared to those predicted by the computational models for a device with the 200 $\mu$m PDMS film containing the oxygen-sensing microparticles. The measured spatial gradients show the spatial variation in oxygen concentration across the width of the cell-channel layer. The measured gradients follow the predicted models closely. The microparticle-containing PDMS films were used only for oxygen transport characterization of the microdevices and were not present in cell culture experiments. Future experiments may incorporate these sensors in PDMS patches in the migration channels to report upon oxygen consumption.

### F. Cell experiments and growth rate comparison

The ability of this device to maintain long-term culture was validated by comparing growth rates of PANC-1 cells in the microfluidic device and in a standard cell culture flask. Cells were maintained within the devices for 8 days under a medium withdrawal rate of 0.1 $\mu$l/min and gas infusion rates through the gas-channel of 5 ml/min.

Calculated growth rate values are shown in Table II. For cells grown in static culture in standard tissue culture flasks under air/5% $CO_2$ and for cells perfused at 0.1 $\mu$l/min within the device under normoxia, there was no statistical difference between their growth rates ($p = 0.2070$). This demonstrates that the perfusion conditions within the device are favorable for normal cell growth. For PANC-1 cells grown within the device under an oxygen gradient with a 1% $O_2$/5% $CO_2$ atmosphere overlying the cell channels and a 21% $O_2$/5% $CO_2$ atmosphere delivered to the vascular channel, and with medium perfusion, the growth rate was

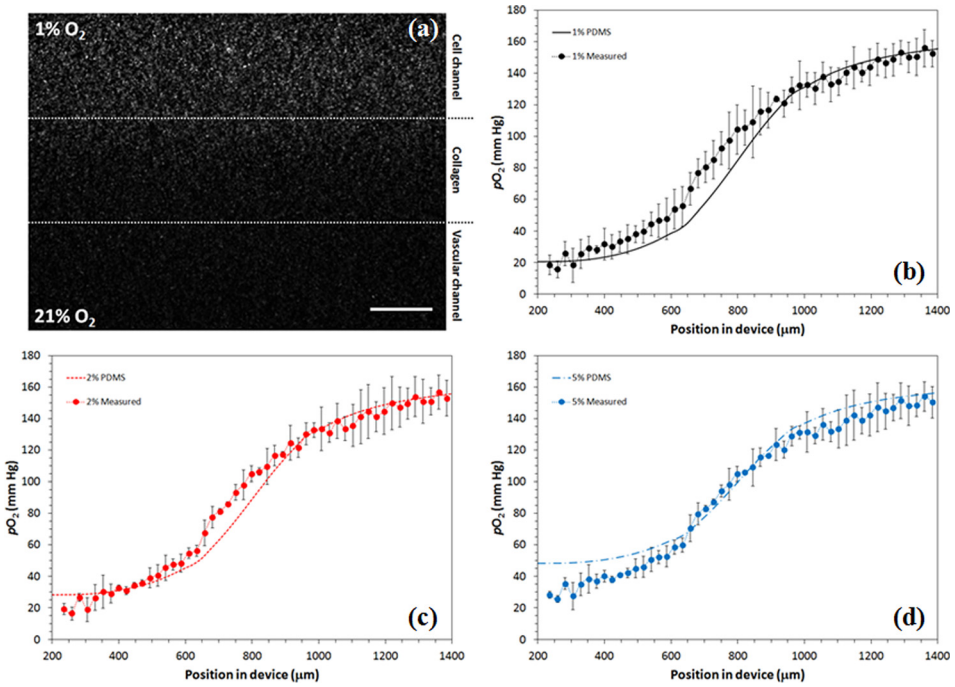


FIG. 5. (a) Fluorescence image of the spatial gradient in fluorescence observed from the oxygen-sensing microparticles embedded within the 200 $\mu$m PDMS film at 6.4× magnification. The gradient was created by infusing 1% $O_2$ through the hypoxia channel and 21% $O_2$ through the normoxia channel. Scale bar marks 200 $\mu$m. (b)–(d) Comparison between predicted oxygen partial pressure gradients (*dashed lines*) and empirical characterizations (*data points*) across the width of the cell-channel layer of the device bound to the PDMS film containing the oxygen-sensing microparticles for (b) 1% $O_2$, (c) 2% $O_2$, and (d) 5% $O_2$. Measured gradient data shown as mean ± standard deviation for the three replicates (n = 3).

TABLE II. Growth rate and doubling times results for cell culture experiments. Data shown as mean ± standard deviation for three replicates (n = 3) after 8 days of culture.

| Culture conditions | Growth rate ($\mu_{net}$, $h^{-1}$) | Doubling time ($\tau_2$, h) |
|---|---|---|
| Flask (normoxia) | 0.0261 ± 0.0036 | 26.9 ± 3.6 |
| Device normoxia | 0.0214 ± 0.0040 | 32.6 ± 6.2 |
| Device hypoxia | 0.0116 ± 0.0011 | 60.3 ± 5.7 |

statistically different ($p = 0.0026$) and less than half that compared to the device under air/5% $CO_2$. The cells were expected to grow at a much slower rate under hypoxia, compared to normoxia. Both normoxia and hypoxia experiments were maintained for up to 8 days, affirming the devices' capability to maintain long-term culture. The only limitation on the duration of these experiments was the inability to count individual cells beyond 8 days as they approached confluency. In theory, slower growing cell lines could be maintained for even longer with replenishment of the medium within the reservoir.

Cell images (Fig. 6) also show the effects of the oxygen atmosphere on the invasion and migration of the cells through the collagen barrier. The images show the cells after staining with crystal violet to enhance their contrast against the transparent PDMS/PS background. The crystal violet stain is retained to a small extent in the collagen gel resulting in the dark regions in these images. The devices were not thoroughly rinsed to remove excess stain to avoid disturbing the cells and collagen membranes. Fig. 6(a) shows the PANC-1 cells after culture within the device for 8 days under a homogenous atmosphere of air/5% $CO_2$. The majority of the cells remained within the cell channel throughout the course of the experiment, stopping their movement at the interface of the collagen barrier. This shows the collagen barrier adheres tightly to the cell surface effectively preventing cell spread into the middle channel. In comparison, Fig. 6(b) shows the cells after 8 days in culture within the device under a continuous $O_2$ gradient established by applying a 1% $O_2$ gas mixture to the cell channel and a 21% $O_2$ mixture to the vascular channel. This image shows breakdown of the collagen barrier with increased cell invasion through this middle channel. In all cases, the cells in each channel can be enumerated by microscopic evaluation. Table III shows the percentage of cells that migrated into the collagen gel channel and the vascular channel. Under conditions where no oxygen gradient was present (air in both channels), few cells migrated into the collagen. Under conditions in which an oxygen gradient was present, i.e., 1% $O_2$ in the cell channel and 21% $O_2$ in the vascular channel, almost a ten-fold higher percentage of cells migrated. The differences in percentage of migrating cells between the uniform and gradient culture was statistically significant

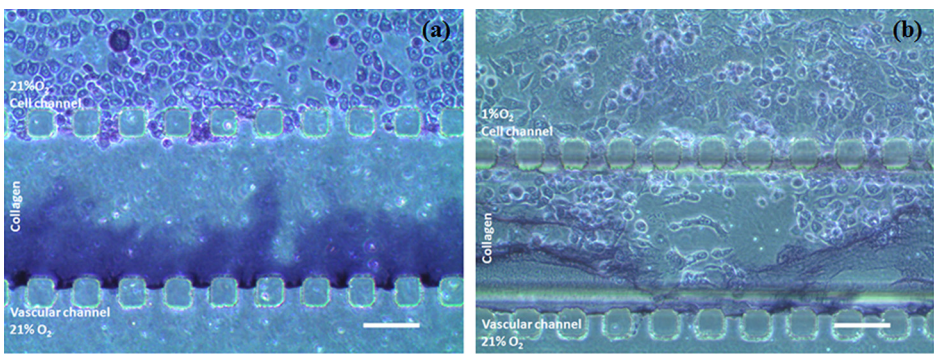


FIG. 6. Phase contrast image of PANC-1 cells within microfluidic device during culture under (a) air/5% $CO_2$ for 8 days and (b) 1%/21% $O_2$ gradient for 8 days at 10× magnification. Scale bar marks 100 μm. Cells were stained with crystal violet to enhance their contrast against the transparent background of the device. The dye also stained the collagen barrier. In (b), the image shows cell migration in response to the created gradient, as well as breakage of the collagen barrier due to the cells' invasion.

TABLE III. Cell migration and intravasation percentage results for cell culture experiments in the tumor-on-a-chip device. Conditions shown reflect oxygen content in the cell channel (C) and vascular channel (V). 5% $CO_2$ is present in all gas mixtures. Data shown as mean ± standard deviation for three replicates (n = 3) after 8 days of culture.

| Culture conditions | Cells in collagen channel (%) | Cells in vascular channel (%) |
|---|---|---|
| Air (C)-Air (V) | 2.4 ± 0.6 | 0.010 ± 0.018 |
| 1% $O_2$ (C)-21% $O_2$ (V) | 20.6 ± 4.0 | 0.029 ± 0.036 |

($p = 0.0206$). In addition, the percentage of cells that crossed the collagen gel and attached to the surface in the vascular channel is very low. These cells model the intravasation process and would be expected to be low in number. With the limited trials performed here, the standard deviations in these data are high; therefore, there was no statistical difference between the two results ($p = 0.6521$). Since the vascular channel also contained flowing medium, some cells emerging into the vascular channel may have been swept away before cell fixing, staining and enumeration. These results demonstrate that the device can indeed be used to generate an oxygen gradient similar to that in the studies of Lo *et al.*,[26] and Adler *et al.*[28] However, in this device, a gradient is applied across an ECM matrix providing an *in situ* invasion assay and mimics the process of both tumor cell invasion and intravasation. None of these earlier devices have this capability. The breakdown of the collagen barrier is expected due to the presence of various proteolytic enzymes excreted by PANC-1 cells including matrix metalloproteinase-2.[52] The staining/rinsing procedure also likely resulted in some mechanical breakdown of the weakened matrix.

The observation of increased migration in the device with cells maintained under 1% oxygen is consistent with an extensive literature, suggesting that hypoxia generates a more aggressive phenotype[53,54] and was found in traditional transwell chamber assays for the PANC-1 cell line.[55–57] It should be noted that in these earlier studies, cells were trypsinized and resuspended in low-serum medium and a chemoattractant was used in each invasion assay.[55–57] In this communication, trypsinization, which may affect viability and invasiveness, was not necessary for the invasion assay nor was a chemoattractant (other than oxygen) added to induce migration.

The device reported herein will be used to systematically study intermittent hypoxia in cancer cell progression. Currently, the literature shows a wide range of cycling times from 10 min hypoxia periods[58] to 1 week hypoxia periods,[59] cycled with similar periods of normoxia. Computer control of our device allows any of these cycling profiles to be investigated. Since cycling compared to chronic hypoxia can induce additional changes in cellular phenotype,[60] the ability to probe a wide range of cycling patterns may be invaluable to defining the mechanistic details of aggressive cancers. In addition to cycles, the oxygen spatial profile across the cell channels can be tailored to probe whether uniform hypoxia across the channel has a different effect on cell invasion as compared to a gradient of hypoxia across the cell channel. This may be used to study metabolic symbiosis in which highly hypoxic cancer cells feed substrates to neighboring cells under more oxygenated conditions.[61] Future features we plan to incorporate into the next generation of the device is to include the ability to co-culture other cells such as fibroblasts and macrophages and line the vascular channel with endothelial cells. This should enhance our abilities to better mimic the *in vivo* cell microenvironment for studies of the metabolic changes in tumor invasion and as a more relevant model for anti-metastatic drug screening.

## IV. CONCLUSIONS

We have developed and characterized a microfluidic platform for studying cancer cell migration under both spatial and temporal changes in oxygenation. The device can create the desired gradients in oxygenation and either chronic or intermittent hypoxia. Finally, the device is capable of sustaining long-term culture of cancer cells and assessing both metastatic and

intravasation potential using gradients in oxygen concentration as its stimulus. Future experiments with this device will compare cell invasion during normoxic and hypoxic culture and assess their viability and protein expression in response to both chronic and intermittent hypoxia.

## ACKNOWLEDGMENTS

We thank Ms. Stephanie Teeter for her technical assistance and Dr. Rex E. Jeffries for valuable discussions. This work was funded by NIH Grant No. R03CA167471.

[1]N. Hiraoka, Y. Ino, S. Sekine, H. Tsuda, K. Shimada, T. Kosuge, J. Zavada, M. Yoshida, K. Yamada, T. Koyama, and Y. Kanai, Br. J. Cancer **103**, 1057–1065 (2010).
[2]R. A. Cairns and R. P. Hill, Cancer Res. **64**, 2054–2061 (2004).
[3]L. I. Cárdenas-Navia, D. Yu, R. D. Braun, D. M. Brizel, T. W. Secomb, and M. W. Dewhirst, Cancer Res. **64**, 6010–6017 (2004).
[4]I. M. Pires, Z. Bencokova, M. Milani, L. K. Folkes, J. L. Li, M. R. Stratford, A. L. Harris, and E. M. Hammond, Cancer Res. **70**, 925–935 (2010).
[5]J. M. Jessup, P. Battle, H. Waller, K. H. Edmiston, D. B. Stolz, S. C. Watkins, J. Locker, and K. Skena, Cancer Res. **59**, 1825–1829 (1999).
[6]I. Almendros, Y. Wang, L. Becker, F. E. Lennon, J. J. Zheng, B. R. Coats, K. S. Schoenfelt, A. Carreras, F. Hakim, S. X. Zhang, R. Farré, and D. Gozal, Am. J. Respir. Crit. Care Med. **189**, 593–601 (2014).
[7]A. Albini and R. Benelli, Nat. Protoc. **2**, 504–511 (2007).
[8]S. C. Oppegard, A. J. Blake, J. C. Williams, and D. T. Eddington, Lab Chip **10**, 2366–2373 (2010).
[9]K. C. Chaw, M. Manimaran, E. H. Tay, and S. Swaminathan, Lab Chip **7**, 1041–1047 (2007).
[10]K. C. Chaw, M. Manimaran, F. E. H. Tay, and S. Swaminathan, Biomed. Microdevices **9**, 597–602 (2007).
[11]S. Chung, R. Sudo, P. J. Mack, C. R. Wan, V. Vickerman, and R. D. Kamm, Lab Chip **9**, 269–275 (2009).
[12]J. Kalchman, S. Fujioka, S. Chung, Y. Kikkawa, T. Mitaka, R. D. Kamm, K. Tanishita, and R. Sudo, Microfluid. Nanofluid. **14**, 969–981 (2013).
[13]N. Li Jeon, H. Baskaran, S. K. Dertinger, G. M. Whitesides, L. Van de Water, and M. Toner, Nat. Biotechnol. **20**(8), 826–830 (2002).
[14]J. Li, L. Zhu, M. Zhang, and F. Lin, Biomicrofluidics **6**(2), 24121–2412113 (2012).
[15]C. P. Huang, J. Lu, H. Seon, A. P. Lee, L. A. Flanagan, H. Y. Kim, A. J. Putnam, and N. L. Jeon, Lab Chip **9**(12), 1740–1748 (2009).
[16]C. T. Kuo, C. L. Chiang, C. H. Chang, H. K. Liu, G. S. Huang, R. Y. Huang, H. Lee, C. S. Huang, and A. M. Wo, Biomaterials **35**(5), 1562–1571 (2014).
[17]J. W. Song, S. P. Cavnar, A. C. Walker, K. E. Luker, M. Gupta, Y. C. Tung, G. D. Luker, and S. Takayama, PLoS ONE **4**(6), e5756 (2009).
[18]S. Bersini, J. S. Jeon, G. Dubini, C. Arrigoni, S. Chung, J. L. Charest, M. Moretti, and R. D. Kamm, Biomaterials **35**(8), 2454–2461 (2014).
[19]R. C. Gunawan, J. Silvestre, H. R. Gaskins, P. J. Kenis, and D. E. Leckband, Langmuir **22**(9), 4250–4258 (2006).
[20]G. Khanal, S. Hiemstra, and D. Pappas, Analyst **139**(13), 3274–3280 (2014).
[21]Y. Qiao and L. Ma, Anal. Chem. **85**(14), 6953–6957 (2013).
[22]G. Khanal, K. Chung, X. Solis-Wever, B. Johnson, and D. Pappas, Analyst **136**(17), 3519–3526 (2011).
[23]H. E. Abaci, R. Devendra, Q. Smith, S. Gerecht, and G. Drazer, Biomed. Microdevices **14**, 145–152 (2012).
[24]S. Martewicz, F. Michielin, E. Serena, A. Zambon, M. Mongillo, and N. Elvassore, Integr. Biol. **4**(2), 153–164 (2012).
[25]J. F. Lo, E. Sinkala, and D. T. Eddington, Lab Chip **10**, 2394–2401 (2010).
[26]J. F. Lo, Y. Wang, A. Blake, G. Yu, T. A. Harvat, H. Jeon, J. Oberholzer, and D. T. Eddington, Anal. Chem. **84**, 1987–1993 (2012).
[27]M. Adler, M. Erickstad, E. Gutierrez, and A. Groisman, Lab Chip **12**, 4835–4847 (2012).
[28]M. Adler, M. Polinkovsky, E. Gutierrez, and A. Groisman, Lab Chip **10**, 388–391 (2010).
[29]K. Funamoto, I. K. Zervantonakis, Y. Liu, C. J. Ochs, C. Kim, and R. D. Kamm, Lab Chip **12**, 4855–4863 (2012).
[30]T. Shiwa, H. Uchida, and K. Tsukada, Am. J. Biomed. Eng. **2**, 175–180 (2012).
[31]G. Mehta, K. Mehta, D. Sud, J. W. Song, T. Bersano-Begey, N. Futai, Y. S. Heo, M. A. Mycek, J. J. Linderman, and S. Takayama, Biomed. Microdevices **9**(2), 123–134 (2007).
[32]B. Mosadegh, B. E. Dabiri, M. R. Lockett, R. Derda, P. Campbell, K. K. Parker, and G. M. Whitesides, Adv. Healthcare Mater. **3**(7), 1036–1043 (2014).
[33]R. W. Kasinskas, R. Venkatasubramanian, and N. S. Forbes, Integr. Biol. **6**(4), 399–410 (2014).
[34]L. Wang, W. Liu, Y. Wang, J. C. Wang, Q. Tu, R. Liu, and J. Wang, Lab Chip **13**, 695–705 (2013).
[35]J. Park, T. Bansal, M. Pinelis, and M. M. Maharbiz, Lab Chip **6**(5), 611–622 (2006).
[36]M. A. Acosta, P. Ymele-Leki, Y. V. Kostov, and J. B. Leach, Biomaterials **30**(17), 3068–3074 (2009).
[37]V. Sunkara, D. K. Park, H. Hwang, R. Chantiwas, S. A. Soper, and Y. K. Cho, Lab Chip **11**(5), 962–965 (2011).
[38]H. Hwang, J. Park, C. Shim, Y. K. Do, and Y. K. Cho, Biomed. Microdevices **15**, 627–634 (2013).
[39]S. G. Charati and S. A. Stern, Macromolecules **31**, 5529–5535 (1998).
[40]K. A. Kneas, J. N. Demas, B. Nguyen, A. Lockhart, W. Xu, and B. A. DeGraff, Anal. Chem. **74**(5), 1111–1118 (2002).
[41]E. R. Carraway, J. N. Demas, B. A. DeGraff, and J. R. Bacon, Anal. Chem. **63**(4), 337–342 (1991).
[42]See supplementary material at http://dx.doi.org/10.1063/1.4898788 showing COMSOL generated oxygen maps and gradients of alternative device designs.
[43]L. Randers-Eichhorn, R. A. Bartlett, D. D. Frey, and G. Rao, Biotechnol. Bioeng. **51**, 466–478 (1996).
[44]R. E. McClelland, J. M. Macdonald, and R. N. Coger, Biotechnol. Bioeng. **82**(1), 12–27 (2003).

[45]S. B. Bambot, R. Holavanahali, J. R. Lakowicz, G. M. Carter, and G. Rao, Biotechnol. Bioeng. **43**, 1139–1145 (1994).
[46]G. T. John, I. Klimant, C. Wittmann, and E. Heinzle, Biotechnol. Bioeng. **81**(7), 829–836 (2003).
[47]C. McDonagh, B. D. MacCraith, and A. K. McEvoy, Anal. Chem. **70**, 45–50 (1998).
[48]A. P. Vollmer, R. F. Probstein, R. Gilbert, and T. Thorsen, Lab Chip **5**, 1059–1066 (2005).
[49]R. D. Braun, J. L. Lanzen, and M. W. Dewhirst, Am. J. Physiol. (Heart Circ. Physiol.) **277**, H551–H568 (1999).
[50]R. A. Cairns, T. Kalliomaki, and R. P. Hill, Cancer Res. **61**, 8903–8908 (2001).
[51]M. W. Dewhirst, Radiat. Res. **172**, 653–665 (2009).
[52]M. G. Binker, A. A. Binker-Cosen, D. Richards, H. Y. Gaisano, R. H. de Cosen, and L. I. Cosen-Binker, Biochem. Biophys. Res. Commun. **393**, 371–376 (2010).
[53]P. Vaupel, A. Mayer, and M. Hockel, Methods Enzymol. **381**, 335–354 (2004).
[54]Z. Yun and Q. Lin, Adv. Exp. Med. Biol. **772**, 41–53 (2014).
[55]S. Cannito, E. Novo, A. Compagnone, C. Valfre, D. Povero, A. Bandino, F. Bozzo, C. Cravanzola, V. Bravoco, S. Colombatto, and M. Parola, Carcinogenesis **29**, 2267–2278 (2008).
[56]J. Lei, J. Ma, Q. Ma, X. Li, H. Liu, Q. Xu, W. Duan, Q. Sun, J. Xu, Z. Wu, and E. Wu, Mol. Cancer **12**, 66 (2013).
[57]Y. Shimojo, M. Akimoto, T. Hisanga, T. Tanaka, Y. Tajima, Y. Honma, and K. Takenaga, Clin. Exp. Metastasis **30**, 143–154 (2013).
[58]N. Chaudry and R. P. Hill, Lab. Invest. **89**, 587–596 (2009).
[59]E. Louie, S. Nik, J. Chen, M. Schmidt, B. Song, C. Pacson, X. F. Chen, S. Park, J. Ju, and E. I. Chen, Breast Cancer Res. **12**, R94 (2010).
[60]V. Malec, O. R. Gottschald, S. Li, F. Rose, W. Seeger, and J. Hänze, Free Radic. Biol. Med. **48**, 1626–1635 (2010).
[61]P. Sonveaux, F. Végran, T. Schroeder, M. C. Wergin, J. Verrax, Z. N. Rabbani, C. J. De Saedeleer, K. M. Kennedy, C. Diepart, B. F. Jordan, M. J. Kelley, B. Gallez, M. L. Wahl, O. Feron, and M. W. Dewhirst, J. Clin. Invest. **118**, 3930–3942 (2008).